

Explainable deep learning for insights in El Nino and river flows

Yumin Liu¹, Kate Duffy², Jennifer G. Dy¹, and Auroop R. Ganguly^{2,3*}

1. SPIRAL Center, Department of Electrical and Computer Engineering, Northeastern University, Boston, Massachusetts 02115, USA

2. Sustainability and Data Sciences Laboratory, Department of Civil and Environmental Engineering, Northeastern University, Boston, Massachusetts 02115, USA

3. Pacific Northwest National Laboratory, Richland, WA 99354

* Corresponding author

The El Nino Southern Oscillation (ENSO) is a semi-periodic fluctuation in sea surface temperature (SST) over the tropical central and eastern Pacific Ocean that influences interannual variability in regional hydrology across the world through long-range dependence or teleconnections¹⁻³. Recent research has demonstrated the value of Deep Learning (DL) methods for improving ENSO prediction as well as Complex Networks (CN) for understanding teleconnections⁴. However, gaps in predictive understanding of ENSO-driven river flows include the black box nature of DL, the use of simple ENSO indices to describe a complex phenomenon and translating DL-based ENSO predictions to river flow predictions. Here we show that eXplainable DL (XDL) methods, based on saliency maps⁵, can extract interpretable predictive information contained in global SST and discover novel SST information regions and dependence structures relevant for river flows which, in tandem with climate network constructions, enable improved predictive understanding. Our results reveal additional information content in global SST beyond ENSO indices, develop new understanding of how SSTs influence river flows, and generate improved river flow predictions with uncertainties. Observations, reanalysis data, and earth system model simulations are used to demonstrate the value of the XDL-CN based methods for future interannual and decadal scale climate projections.

Main text

The El Nino-Southern Oscillation (ENSO) is a primary mode of interannual weather variability around the globe. ENSO modulates flood timings in Africa¹, interannual variability of flow in the Ganges, the Amazon, and the Congo rivers^{2,3}, and has significant influences on regional climate and hydrologic patterns around the globe. A predictive understanding of ENSO is thus of economic and societal importance. However, and our ability to predict ENSO with physics-based numerical simulations or data-driven models at interannual, decadal, and multidecadal time horizons have remained relatively poor⁶, which has in turn hindered our ability to predict regional patterns of hydrometeorology.

Some challenges in ENSO forecasting may be traced back to overly reductive models, such as the relatively arbitrary rectangular regions that determine ENSO indices. Studies have suggested that ENSO is part of a larger system of interrelated SST oscillations which may co-impact regional hydrometeorology⁷. Further, our understanding of physical mechanisms⁸ along with data-driven methods⁹ suggest that the relationships between ENSO and river flows may be highly nonlinear. The resulting complexity of the earth system calls for methods that can leverage complete information content from global SST data and identify complex geographic dependence structures, which include both proximity-based dependence and long-range teleconnections. Fig. 1 shows SST anomalies in year 2008 when there was a cool year (La Nina phenomenon), while Fig. S2(a) and S2(b) show SST anomalies in a warm year (El Nino) and a neutral year, respectively. The relationships between river flows and ENSO indices indicate the possibility of significant nonlinear dependency (Table S3 and Fig. S6 and S7).

Commonly used methods to identify dependencies among climate variables include visual comparison¹⁰, correlation¹¹, mutual information⁹, coefficient of determination¹², and weights in (sparse) linear regression^{13,14}. These methods often require heuristic expertise in selecting features and can be difficult to extend to more complex features such as three-dimensional spatiotemporal features. In the recent years, deep learning methods have seen preliminary success in climate science, meteorology, and hydrology, resulting in improved predictive skills and development of new methods to investigate the spatiotemporal dependencies^{4,15}. Furthermore, methods for interpretation and explanation of deep neural networks, such as saliency maps, can be adapted to climate problems to analyze relevant (SST) regions

resulting in understandable predictive information for regional climate and hydrology. Simonyan et al.⁵ initially proposed the saliency map method as a visualization technique to explain the neural network function mapping, specifically, the extent to which inputs contribute to network output. Due to their effectiveness, explainable deep learning methods have been widely applied to the geosciences and especially to understand climate science and translate to impacts, for example, in spatial drought prediction¹⁶, satellite-based PM2.5 (air pollution) measurements¹⁷, crop yields¹⁸, species distribution models¹⁹, analysis of hailstorms²⁰, hydro-climatological process modeling²¹, precipitation quality control²² and climate drivers for global temperature²³, and to localize pest insects in agricultural application²⁴. Ham et al.⁴ used saliency map to analyze which regions contributed most in predicting the Nino3.4 index using their neural network. Similarly, Mahesh et al. ²⁵ applied saliency maps to find the important geographic regions for predicting Nino3.4 index.

Here we address the problem of developing explainable predictive insights relating to the ENSO phenomenon. Our approach is based on an eXplainable Deep Learning (XDL) solution ⁵ that concurrently uses convolutional neural networks (CNN) for prediction of river flow time series and saliency maps to explain the results by highlighting the relative importance of the spatiotemporal SST data. Our implicit hypothesis is that the XDL approach will lead to advances in predictive skills of river flows by considering the information content in the entire SST map, which should exceed the information content of ENSO indices. Furthermore, the XDL approach may lead to new discoveries of robust SST teleconnections with each other and with river flows, which in turn would further explain the gains in predictive skills. We develop correlation-based metrics to quantify SST autocorrelations and teleconnections either owing to known proximity-based spatial correlations or owing to known long-range spatial dependence. The approaches are developed for proxy observations (reanalysis) datasets as well as earth system model (ESM) simulated Coupled Modeling Intercomparison Project phase 5 (CMIP5) data, both for assessments of historical skills as well as for use in future projections of teleconnections and river flows which represent a major gap in current generation earth system models²⁶⁻²⁸.

Results

We trained a CNN (Fig. S10) to predict monthly Amazon and Congo River flow from monthly SST derived from Earth System Models (ESM) and reanalysis data. We compared the skill to that of an ensemble of ML models, which predicted river flow using only indices calculated from the Nino 3.4 region (5°S-5°N, 170°W-120°W). We found that models using the larger SST area (41.5°S-37.5°N, 50.5°E-9.5°W) outperformed models using the ENSO indices for prediction of three-month rolling mean river flows (Fig. 2). The CNN ingesting more SST information also outperformed the historical climatological mean as a predictor of Amazon River flow. This suggests the larger SST region was useful for capturing the phase and amplitude of annual river flow fluctuations as well as components of interannual variation. Our experiments suggest that information with predictive power on the interannual variability of the Amazon River flow was either not fully expressed in the ENSO index, or else was not captured by the ensemble of ML models (linear regression, lasso regression, ridge regression, elastic net regression, random forest regression, and feed forward dense neural network, or DNN, regression). A full comparison of RMSE for river flow prediction using indices and larger area SST is presented in Table S2.

The task of predicting Congo River flow was more challenging, perhaps influenced by the more extensive management of the Congo River basin compared to the Amazon River basin. Predictions based on historical climatological mean resulted in lower RMSE than any candidate model for the Congo River. Deeper analysis of CNN performance and historical average (presented in Tables S4 and S5) suggest that the methods compare differently when different aspects of performance (linear/nonlinear correlation, seasonal/yearly, extremes, etc.) are examined.

We used a cyclical saliency map method to identify important spatial areas for the network to make predictions of river flows (Fig. 3). From the saliency maps we discover that the predictive power of ESMs comes mainly from the ENSO and the Indian Ocean Dipole (IOD) regions, suggesting a strong link between these two phenomena and a co-impact on regional hydrology. Fig. 3(a) shows that the dominant salient areas for Amazon River flow prediction are in tropical Pacific and Indian Oceans. Fig. 3(c) shows similar patterns but with less strong and smaller salient areas for Congo River flow. When using reanalysis data (Fig. 3(b) and 3(d)), the saliency maps are much more diffused, suggesting that the CNN

model does not pick up any strong relationships between the predictor and predictand. One potential reason is that the reanalysis data are interpolated from very sparse observations and thus have diminished predictive power. The yearly cyclical saliency maps and seasonal saliency maps are also presented in the Fig. S2-S5. Whereas saliency maps can be used to verify the physically reasonable relationships that are learned as well as to discover new relationships, our hypothesis can be confirmed by examining the degree to which known oceanic regions that correspond to the ENSO region, as well as oceanic regions that correlate with the ENSO region, are triggered by the saliency maps as contributors to the information content.

Complex network theory provides a complementary tool to investigate the short and long-distance relationships in earth systems, such as teleconnections associated with the ENSO phenomenon that are indicated by our results. We analyzed the correlation structure of global SST data by constructing degree maps for reanalysis and ESM SST (Fig. 4). We quantified temporal correlation by calculating Pearson's correlation coefficient between every pair of locations in the ocean. The degree of each geographical location is the number of edges connected to this location, where an edge exists if the correlation is larger than a threshold c_1 . We also set a second correlation threshold c_2 and distance threshold d to define a teleconnection. We define that there is a teleconnection between two locations if their distance is larger than d km and the correlation is larger than c_2 .

We find that ESM SST has high degree values over a large area, indicating that the SST are highly correlated through both proximity-based correlations and teleconnections. There are many teleconnections between tropical Pacific Ocean, Indian Ocean, and even Atlantic Ocean, and they are largely concentrated around the equator (Fig. 4(a)). The teleconnections remain strong when the correlation threshold is increased (Fig. 4(c)). This pattern is reflected in the histogram of edges, which shows the degree distribution (Fig. 4(e) and 4(g)). There are many edge counts for long distances, which demonstrate the multicollinearity between SST regions. In contrast, the histograms of edges for reanalysis data (Fig. 4(b) and 4(d)) show fewer long-distance connections for a low correlation threshold, and negligible long-distance connections with a high correlation threshold. These results indicate a weaker correlation structure in reanalysis SST compared to ESM SST.

Histograms of connection distance in each of ESMs indicate qualitative differences in the correlation structures of the models (Fig. S8 and S9); some exhibit a single peak corresponding to proximity-based correlations (e.g. Fig. S8(a)), while others also exhibit clusters of long-range connections (e.g. Fig. S8(f)). Models also vary in the rapidity of decay of proximity-based correlations with increasing distance. These attributes of these plots indicate distinct spatiotemporal correlation structures among the climate models.

Conclusion

ENSO is a complex spatiotemporal process with global impacts on SST and the flows of large rivers globally, especially around the tropics and subtropics. In this work we combined ML methods and interpretive techniques to obtain gains in predictive power and make new discoveries about dependence structures and teleconnections in global SST data. Although researchers often analyze the relationship between ENSO indices and the other climate variables, our results indicate that information outside of the canonical ENSO region can help to predict regional hydrology better than some reduced representations based on hand-selected features. They suggest that additional data and data-driven technologies could lead to a better understanding of mechanisms and the flow of causality in earth systems, as well as to informed climate adaptation through augmented projections of river flow for future climate scenarios.

Methods

Datasets

We obtained monthly sea surface temperature datasets from ESM simulations and reanalysis models. The ESM datasets are downloaded from NASA Earth eXchange (NEX, <https://registry.opendata.aws/nasanex/>, last access May 2021). From the full set of Coupled Model Intercomparison Project Phase 5 (CMIP5) ESMs by various institutes, we discard those which have some months missing, leaving 32 ESMs. The CMIP5 historical forcing experiment spans from January 1950 to December 2005, or 672 months in total. This ESM dataset covers the whole globe with a spatial

resolution of 1° longitude by 1° latitude (approximate 100km by 100km) with longitudes range from 0.5°E to 359.5°E, and latitudes from 87.5°N to 87.5°S. The ESM names are shown in Table S1.

In addition to ESM simulation datasets, we also use reanalysis datasets which are combinations of sparse on-site observation with other sources (such as remote sensing and satellite imaging) to produce gridded data. It is common to use reanalysis data as the proxy of true observational data because the site-based observational data are very sparse and not gridded. We use three reanalysis datasets in the experiment as predictors: Hadley-OI SST dataset²⁹, COBE SST dataset³⁰ and ERSSTV5 dataset³¹.

The merged Hadley-OI SST dataset (<https://climatedataguide.ucar.edu/climate-data/merged-hadley-noaa-oi-sea-surface-temperature-sea-ice-concentration-hurrell-et-al-2008>) is a combination of two reanalysis datasets: HadISST1³² and NOAA OI.v2³³. The HadISST1 dataset is derived gridded, bias-adjusted in situ observations, and the NOAA OI.v2 dataset combines in situ and satellite-derived SST data. The resulting Hadley-NOAA-OI dataset contains monthly mean sea surface temperature from year 1870 to 2020 with a spatial resolution of 1° longitude by 1° latitude.

The COBE SST dataset (<https://climatedataguide.ucar.edu/climate-data/sst-data-cobe-centennial-situ-observation-based-estimates>) are centennial in situ observation-based estimation that combines SSTs from International Comprehensive Ocean-Atmosphere Data Set (ICOADS)³⁴ release 2.0, the Japanese Kobe collection and reports from ships and buoys. ICOADS is the most comprehensive archive of global marine surface climate observations available, but the data coverage is sparse and neither gridded nor corrected. These datasets were gridded using optimal interpolation. The resulting COBE dataset contains monthly mean sea surface temperature from 1891 to 2020 with a spatial resolution of 1° longitude by 1° latitude.

The NOAA extended reconstruction SSTs version 5 (ERSSTV5) dataset (<https://climatedataguide.ucar.edu/climate-data/sst-data-noaa-extended-reconstruction-ssts-version-5-ersstv5>) is based on statistical interpolation of the ICOADS release 3.0 data and Argo (<https://argo.ucsd.edu/>) float data. The resulting ERSSTV5 dataset contains monthly mean sea surface temperature from year 1854 to 2019 with a spatial resolution of 2° longitude by 2° latitude.

These datasets have different time spans and spatial resolutions. We performed preprocessing to align the coordinates, interpolate to the same spatial resolution, and select the common time span. Missing values are filled with 0. After preprocessing, the resulting reanalysis input has 3 channels corresponding to the 3 reanalysis datasets described above with a spatial resolution of 1° longitude by 1° latitude. We extract the region with latitude from 37.5°N to 42.5°S , and longitude from 50.5°E to 0.5°W , roughly covering most of low latitude Pacific Ocean and Indian Ocean. The resulting input image size is 80×300 height by width.

The river flow dataset was obtained from UCAR (A. Dai 2017) and can be downloaded from UCAR Research Data Archive website (<https://rda.ucar.edu/datasets/ds551.0/index.html>, last accessed January 2021). The dataset contains monthly runoff (m^3/month) for many rivers in the world. The record for Amazon River was observed in the downstream Amazon River at a station in Obidos, Brazil from December 1927 to October 2018, totally 1091 months available. The record for Congo River was measured at a station in Kinshasa, Congo from January 1903 to January 2011, totally 1296 months. We calculated moving mean river flow using a moving window of length 3 months and used it as the smoothed river flow for the third month.

For both predictor (SST) and predictand (river flow) our monthly data span from January 1950 to December 2005. Of this totally 672 months, we use the first 600 months as our training data, the following 36 months as our validation data to select best parameters for the model, and the last 36 months (January 2003 to December 2005) as the test data.

Neural Network Model

The CNN used in this paper consists of 4 convolutional layers and 3 fully connected layers. The number of output channels for each convolutional layer is 32, 32, 64 and 64, respectively. They all have stride 1. The filter sizes in the first three layers are 3×3 , and for the fourth layer, it is 1×1 . All convolutional layers are followed by a ReLU activation and a 2D max pooling layer with size 2×2 and stride 2×2 . For the fully connected layers, the number of output feature for each layer is 128, 64 and 1, respectively. The input image size is $80 \times 300 \times C$ with different number of channels C . For all ESMs as input, $C=32$. For all reanalysis input, $C=3$. For mean ESMs or mean reanalysis as input, $C=1$. The network output is a scalar.

We set the training batch size as 64 and use Adam optimizer with initial learning rate 5×10^{-5} and weight decay 1×10^{-4} . We use squared loss function and the network tries to minimize the loss function:

$\frac{1}{T} \sum_{t=1}^T (f(X_t, w) - y_t)^2$, where T is the number of training samples, $X_t \in R^{W \times H \times C}$ is the t -th input with width W , height H and number of channels C , y_t is the t -th ground truth target, $w = \{w_1, \dots, w_L\}$ is the set of weights from all layers. The network output $f(X_t, w) = f_L(f_{L-1}(\dots f_1(X_t, w_1)))$, where $f_l(\cdot, w_l)$ is the mapping function for the l -th layer in the neural network.

Saliency Map and Cyclical Saliency Map (Cyclic-SM)

The saliency map for a CNN is the derivative of the network output y with respect to the input $X: S = \frac{\partial y}{\partial X}$, where S is the same size as the input⁵. The magnitude of elements S_{ijk} in S reflects how important the corresponding input pixel X_{ijk} (where i, j, k is the index of the width, height and channel of X) is to the output prediction. For climate variables viewed as images in different time frame, they usually exhibit some (irregular) periodicity in the time. We can utilize this property to enhance the saliency map by superimposing individual saliency maps to form a conglomerate saliency map. Specifically, we define the Cyclic-SM with a cycle M as: $S^c = \frac{1}{K+1} \sum_{k=0}^K S_{t+kM} = \frac{1}{K+1} \sum_{k=0}^K \frac{\partial y_{t+kM}}{\partial X_{t+kM}}$, where $K = \left\lfloor \frac{T-t}{M} \right\rfloor$ is the number of individual saliency maps in the cycle.

The averaging nature of the Cyclic-SM makes it more robust to gradient fluctuation and noise compared to an ordinary saliency map. In addition, Cyclic-SMs are meaningful in climate context. For example, for monthly data, $M=12$ corresponds to a natural month cycle (January, February, ..., December). And we further define seasonal and yearly Cyclic-SM as the sum of saliency maps of the corresponding months. We can calculate different Cyclic-SMs with different cycles depending on the specific purpose and climate data used. For example, we can get daily, monthly, seasonal, annual or other Cyclic-SMs to analyze the dependencies between climate variables in different time scales.

Data availability

All data used are publicly available.

Code availability

Codes are available online at <https://github.com/yuminliu/SaliencyMap> (currently private).

References

1. Ficchì, A. & Stephens, L. Climate Variability Alters Flood Timing Across Africa. *Geophysical Research Letters* **46**, 8809–8819 (2019).
2. Whitaker, D. W., Wasimi, S. A. & Islam, S. The El Niño southern oscillation and long-range forecasting of flows in the Ganges. *International Journal of Climatology* **21**, 77–87 (2001).
3. Amarasekera, K., Robert Lee, Earle Williams, & Elfitah, Eltahir. ENSO and the natural variability in the flow of tropical rivers. *Journal of Hydrology* (1997).
4. Ham, Y.-G., Kim, J.-H. & Luo, J.-J. Deep learning for multi-year ENSO forecasts. *Nature* **573**, 568–572 (2019).
5. Simonyan, K., Vedaldi, A. & Zisserman, A. Deep Inside Convolutional Networks: Visualising Image Classification Models and Saliency Maps. *arXiv:1312.6034 [cs]* (2014).
6. Michael McPhaden, Stephen Zebiak, & Michael Glantz. ENSO as an Integrating Concept in Earth Science. *Science* **314**, 1740–1745 (2006).
7. Cai, W., Rensch, P. van, Cowan, T. & Hendon, H. H. Teleconnection Pathways of ENSO and the IOD and the Mechanisms for Impacts on Australian Rainfall. *Journal of Climate* **24**, 3910–3923 (2011).
8. Zhang, W., Jiang, F., Stuecker, M. F., Jin, F.-F. & Timmermann, A. Spurious North Tropical Atlantic precursors to El Niño. *Nat Commun* **12**, 3096 (2021).
9. Khan, S. *et al.* Nonlinear statistics reveals stronger ties between ENSO and the tropical hydrological cycle. *Geophysical Research Letters* **33**, (2006).
10. Abram, N. J. *et al.* Coupling of Indo-Pacific climate variability over the last millennium. *Nature* **579**, 385–392 (2020).
11. Déry, S. J. & Wood, E. F. Decreasing river discharge in northern Canada. *Geophysical Research Letters* **32**, (2005).
12. Siam, M. S. & Eltahir, E. a. B. Explaining and forecasting interannual variability in the flow of the Nile River. *Hydrology and Earth System Sciences* **19**, 1181–1192 (2015).
13. Chatterjee, S., Steinhaeuser, K., Banerjee, A., Chatterjee, S. & Ganguly, A. Sparse Group Lasso: Consistency and Climate Applications. in *Proceedings of the 2012 SIAM International Conference on*

Data Mining 47–58 (Society for Industrial and Applied Mathematics, 2012).

doi:10.1137/1.9781611972825.5.

14. Liu, Y., Chen, J., Ganguly, A. & Dy, J. Nonparametric Mixture of Sparse Regressions on Spatio-Temporal Data – An Application to Climate Prediction. 9 (2019).
15. McGovern, A., Ii, D. J. G., Williams, J. K., Brown, R. A. & Basara, J. B. Enhancing understanding and improving prediction of severe weather through spatiotemporal relational learning. *Mach Learn* 24 (2014).
16. Dikshit, A. & Pradhan, B. Interpretable and explainable AI (XAI) model for spatial drought prediction. *Science of The Total Environment* 801, 149797 (2021).
17. Yan, X. *et al.* A Spatial-Temporal Interpretable Deep Learning Model for improving interpretability and predictive accuracy of satellite-based PM2.5. *Environmental Pollution* 273, 116459 (2021).
18. Wolanin, A. *et al.* Estimating and understanding crop yields with explainable deep learning in the Indian Wheat Belt. *Environ. Res. Lett.* 15, 024019 (2020).
19. Ryo, M. *et al.* Explainable artificial intelligence enhances the ecological interpretability of black-box species distribution models. *Ecography* 44, 199–205 (2021).
20. Gagne, D. J., Haupt, S. E., Nychka, D. W. & Thompson, G. Interpretable Deep Learning for Spatial Analysis of Severe Hailstorms. *Monthly Weather Review* 147, 2827–2845 (2019).
21. Chakraborty, D., Başağaoğlu, H. & Winterle, J. Interpretable vs. noninterpretable machine learning models for data-driven hydro-climatological process modeling. *Expert Systems with Applications* 170, 114498 (2021).
22. Sha, Y., Ii, D. J. G., West, G. & Stull, R. Deep-Learning-Based Precipitation Observation Quality Control. *Journal of Atmospheric and Oceanic Technology* 38, 1075–1091 (2021).
23. Labe, Z. M. & Barnes, E. A. Detecting Climate Signals Using Explainable AI With Single-Forcing Large Ensembles. *Journal of Advances in Modeling Earth Systems* 13, e2021MS002464 (2021).
24. Liu, Z., Gao, J., Yang, G., Zhang, H. & He, Y. Localization and Classification of Paddy Field Pests using a Saliency Map and Deep Convolutional Neural Network. *Sci Rep* 6, 20410 (2016).
25. Mahesh, A. *et al.* Forecasting El Niño with Convolutional and Recurrent Neural Networks. 5.

26. Bellenger, H., Guilyardi, E., Leloup, J., Lengaigne, M. & Vialard, J. ENSO representation in climate models: from CMIP3 to CMIP5. *Clim Dyn* **42**, 1999–2018 (2014).
27. Beobide-Arsuaga, G., Bayr, T., Reintges, A. & Latif, M. Uncertainty of ENSO-amplitude projections in CMIP5 and CMIP6 models. *Clim Dyn* **56**, 3875–3888 (2021).
28. McKenna, S., Santoso, A., Gupta, A. S., Taschetto, A. S. & Cai, W. Indian Ocean Dipole in CMIP5 and CMIP6: characteristics, biases, and links to ENSO. *Sci Rep* **10**, 11500 (2020).
29. Hurrell, J. W., Hack, J. J., Shea, D., Caron, J. M. & Rosinski, J. A New Sea Surface Temperature and Sea Ice Boundary Dataset for the Community Atmosphere Model. *Journal of Climate* **21**, 5145–5153 (2008).
30. Ishii, M., Shouji, A., Sugimoto, S. & Matsumoto, T. Objective analyses of sea-surface temperature and marine meteorological variables for the 20th century using ICOADS and the Kobe Collection. *International Journal of Climatology* **25**, 865–879 (2005).
31. Huang, B. *et al.* Extended Reconstructed Sea Surface Temperature, Version 5 (ERSSTv5): Upgrades, Validations, and Intercomparisons. *Journal of Climate* **30**, 8179–8205 (2017).
32. Rayner, N. A. *et al.* Global analyses of sea surface temperature, sea ice, and night marine air temperature since the late nineteenth century. *Journal of Geophysical Research: Atmospheres* **108**, (2003).
33. Reynolds, R. W., Rayner, N. A., Smith, T. M., Stokes, D. C. & Wang, W. An Improved In Situ and Satellite SST Analysis for Climate. *Journal of Climate* **15**, 1609–1625 (2002).
34. Berry, D. I. & Kent, E. C. A New Air–Sea Interaction Gridded Dataset from ICOADS With Uncertainty Estimates. *Bulletin of the American Meteorological Society* **90**, 645–656 (2009).

Acknowledgements

This work was funded by the National Science Foundation through grants (CyberSEES, Big Data) awarded to ARG.

Author contributions

YL performed the analysis and wrote the first draft of the paper. KD helped define the problem and co-wrote the paper with YL and ARG. ARG and JD defined the problem. All authors interpreted the results and contributed to the writeup.

Competing interests

The authors declare no competing interests.

Materials & Correspondence

Correspondence to Auroop R. Ganguly, auroop@gmail.com

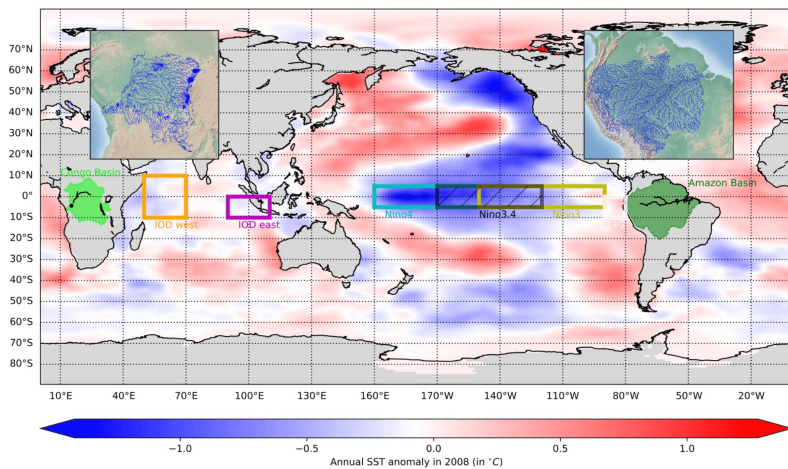
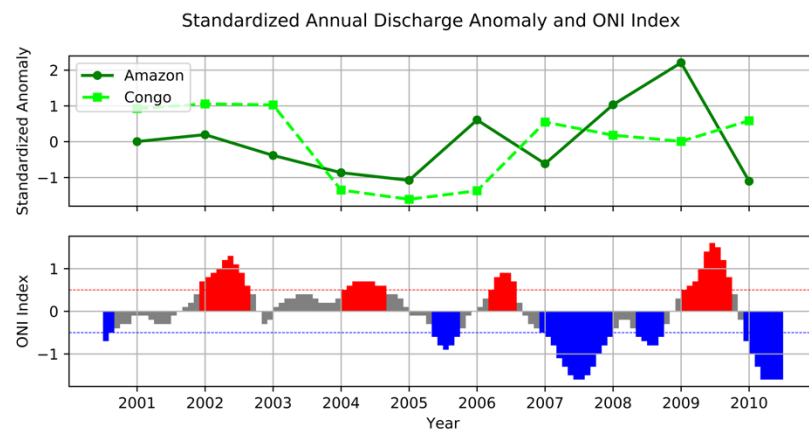
a**b**

Figure 1. Global sea surface temperature fluctuations including the El Nino Southern Oscillation impact interannual variability in the flow of large rivers such as Amazon and Congo. a, Regions for calculating ENSO indices (Nino 1+2, Nino 3, Nino 3.4 and Nino 4) and Indian Ocean dipole mode index (DMI), and two hydrological regions (Amazon river basin and Congo river basin). The colors shown on the ocean is the annual SST anomaly in year 2008. **b,** Time series of standardized annual river flow in m^3/s for Amazon (green) and Congo (lime) and monthly Oceanic Nino Index (ONI) in the Nino 3.4 region at the same time-period. The ONI data are from United States Climate Prediction Center (NOAA 2021). Warm (red) and cold (blue) periods show months that are higher than $+0.5^{\circ}\text{C}$ or lower than -0.5°C threshold for minimum of five consecutive months. A warm/cold year is a year when warm/cold anomaly months dominate, and a neutral year is a year that is neither a warm nor a cold year. For Amazon, the river flow decreases during the warm period and increases during the cold period. However, the relations between Congo River flow and ONI are more complicated and not obvious.

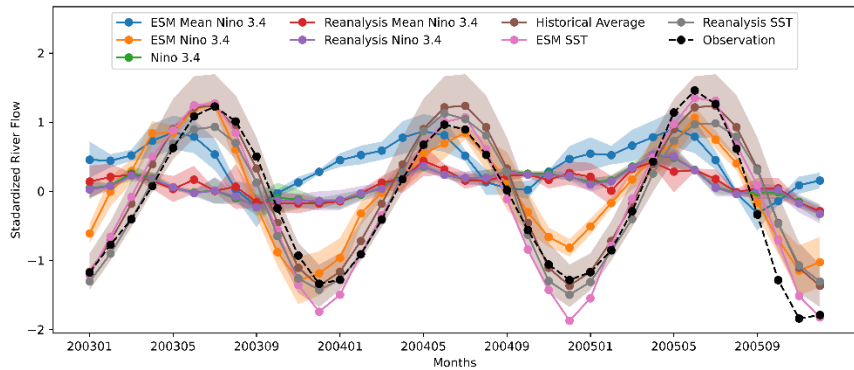
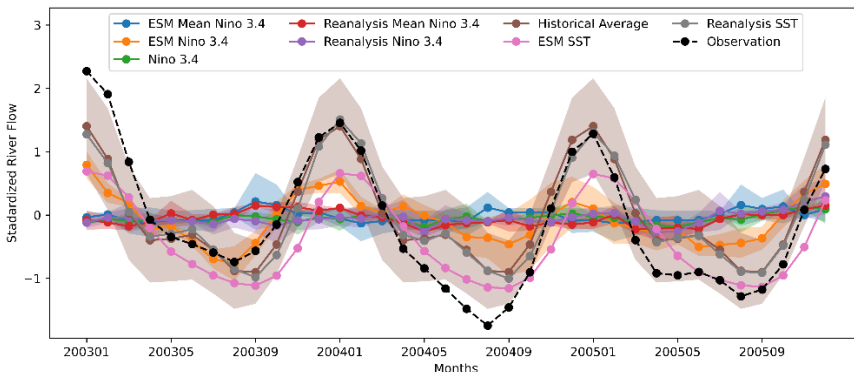
a**b**

Figure 2. Predictions of the interannual variability of the Amazon and Congo rivers based on observed and model-simulated sea surface temperatures compared with climatology. River flow ground truth observations (black) and predictions using different predictors from January 2003 to December 2005 for Amazon (a) and Congo (b) river. The predictors are mean Nino 3.4 calculated from 32 ESMs (ESM Mean Nino 3.4), Nino 3.4 calculated from each of 32 ESMs (ESM Nino 3.4), Nino 3.4 index from NOAA (Nino 3.4), Nino 3.4 calculated from 3 reanalysis (Reanalysis Mean Nino3.4), Nino 3.4 calculated from each of 3 Reanalysis (Reanalysis Nino 3.4), SST from 32 ESMs (ESM SST, light purple) and SST from 3 reanalysis (Reanalysis SST, gray). The brown line is the historical average prediction result. For models using ENSO index as predictor, we applied six models (linear regression, ridge regression, elastic net regression, random forest regression and DNN regression) and use their ensemble as the final prediction. The shaded areas are 1 standard deviation for ensemble methods and historical averaging.

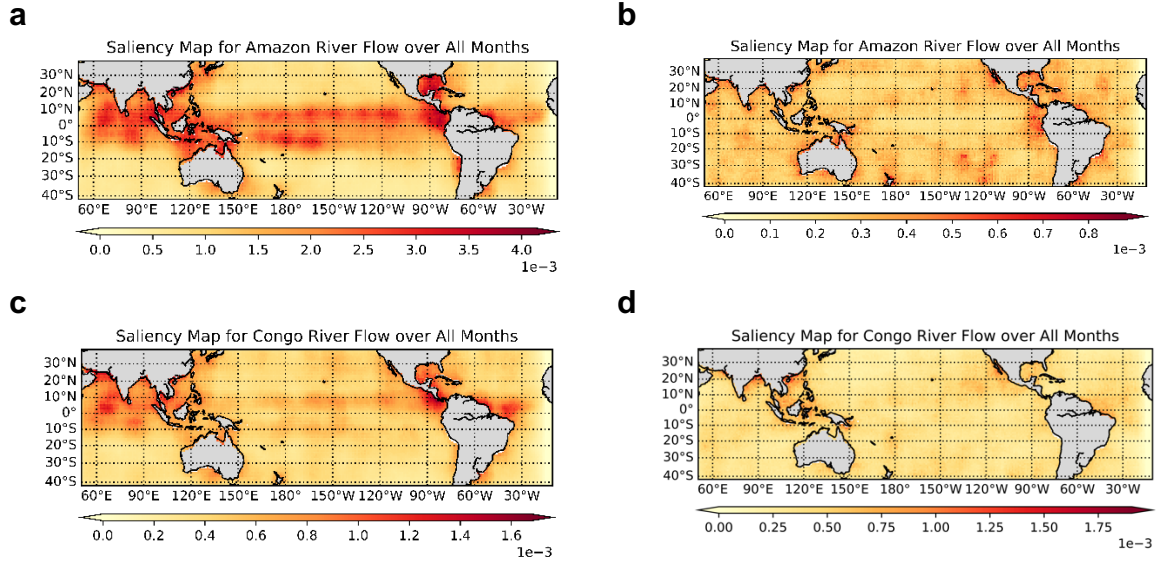


Figure 3. Explainable deep learning showing saliency maps for predictive understanding with the network model representations. (a,b), Saliency Map for Amazon river flow prediction using ESMs (a) and reanalysis (b) SST, respectively. (c,d), Saliency Map for Congo river flow prediction using ESMs (c) and reanalysis (d) SST, respectively. When using ESM SST as predictor, the salient areas mainly lie in the tropical Pacific and Indian Ocean, but they are much more diffused when using reanalysis SST.

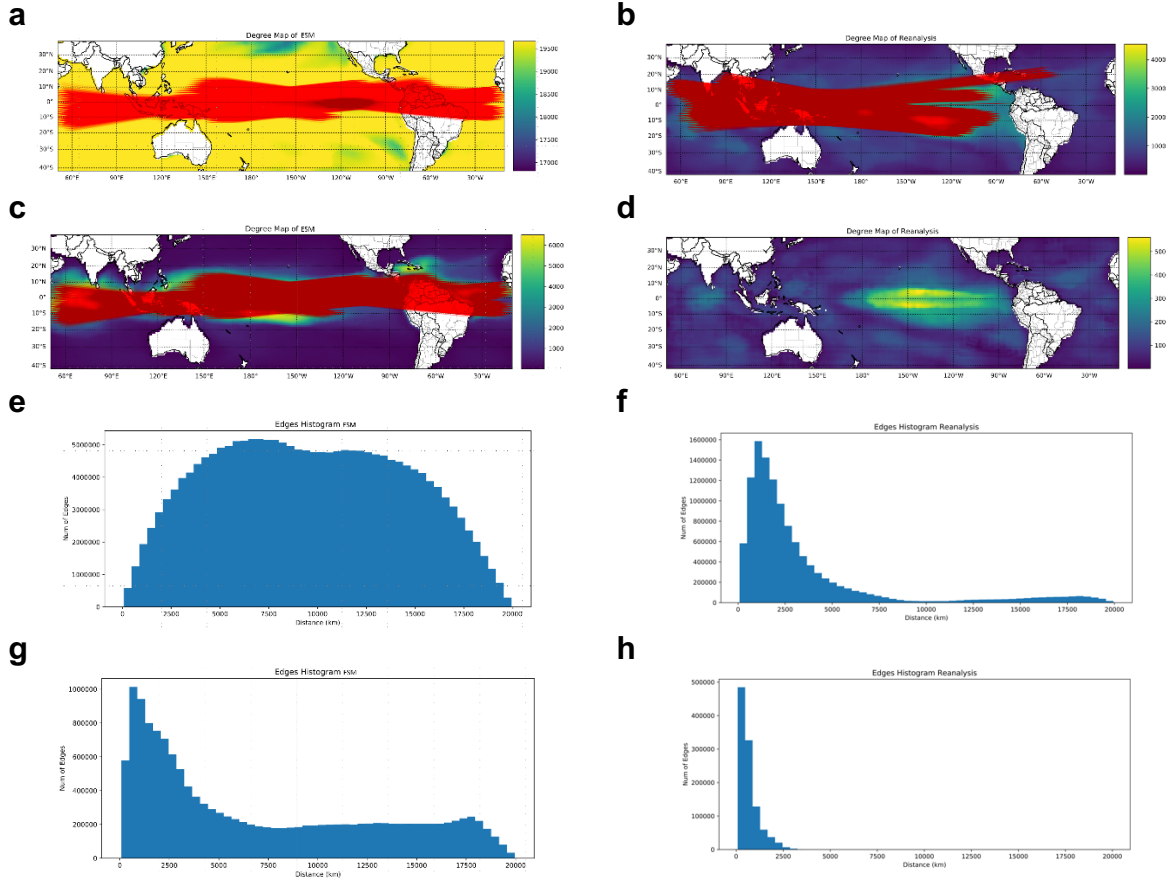
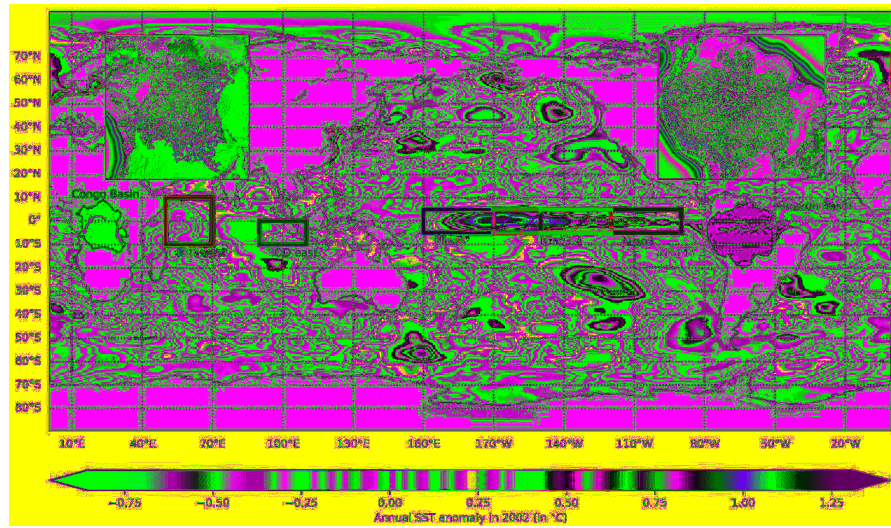


Figure 4. Teleconnections in space and time based on reanalysis and model-simulated link strengths and degree maps used to construct and interpret complex networks in climate. a,c, Degree map and teleconnections for mean ESM SSTs. **(a)**, correlation threshold equal to 0.5 and 0.9 for degree and teleconnection. **c**, correlation threshold equal to 0.9 and 0.9 for degree and teleconnection. **b,d**, Degree map and teleconnections for mean Reanalysis SSTs. **b**, correlation threshold equal to 0.5 and 0.5 for degree and teleconnection. **d**, correlation threshold equal to 0.9 and 0.9 for degree and teleconnection. We show teleconnections with distance larger than 19000km and 15000km for ESM and Reanalysis SST, respectively. **e,g**, the histogram of edges using correlation threshold 0.5 and 0.9 for mean ESM SST. **f,h**, the histogram of edges using correlation threshold 0.5 and 0.9 for mean Reanalysis SST.

a



b

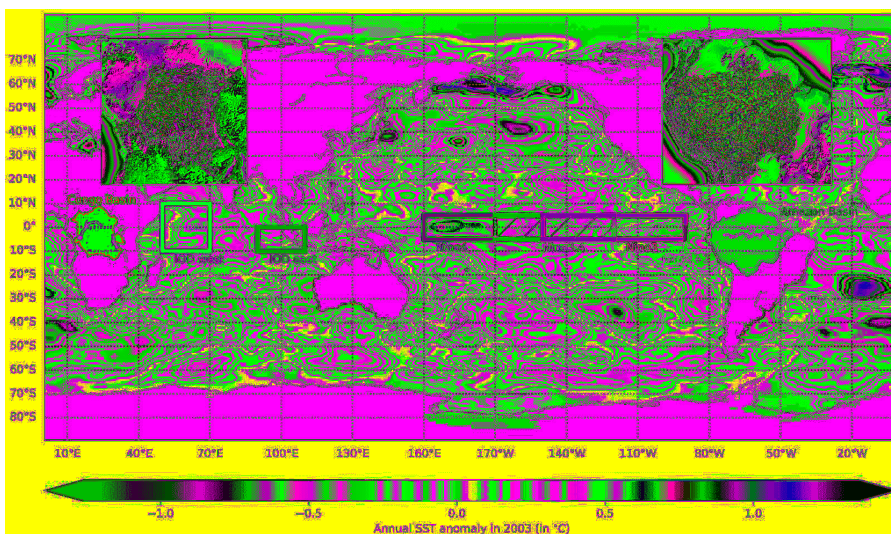


Figure S1. Illustration of SST anomaly in a warm (El Niño) year (a, year 2002) and a neutral year (b, year 2003). In a, although the SST anomaly around the Niño regions are positive (warm), there are large part of ocean with negative SST anomaly.

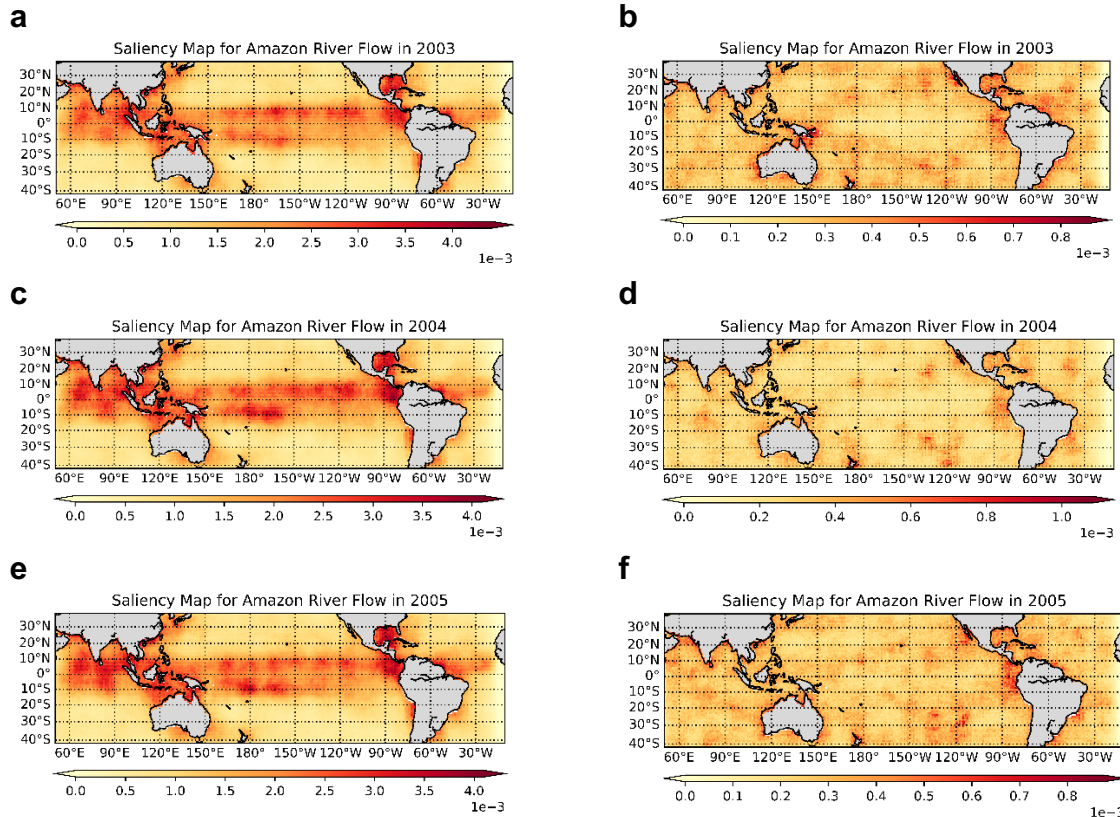


Figure S2. Yearly cyclical saliency maps for predicting Amazon river flow using ESM (a,c,e) and reanalysis (b,d,f) SST. The yearly cyclical saliency maps are calculated as the mean of saliency maps of the 12 months in the corresponding year.

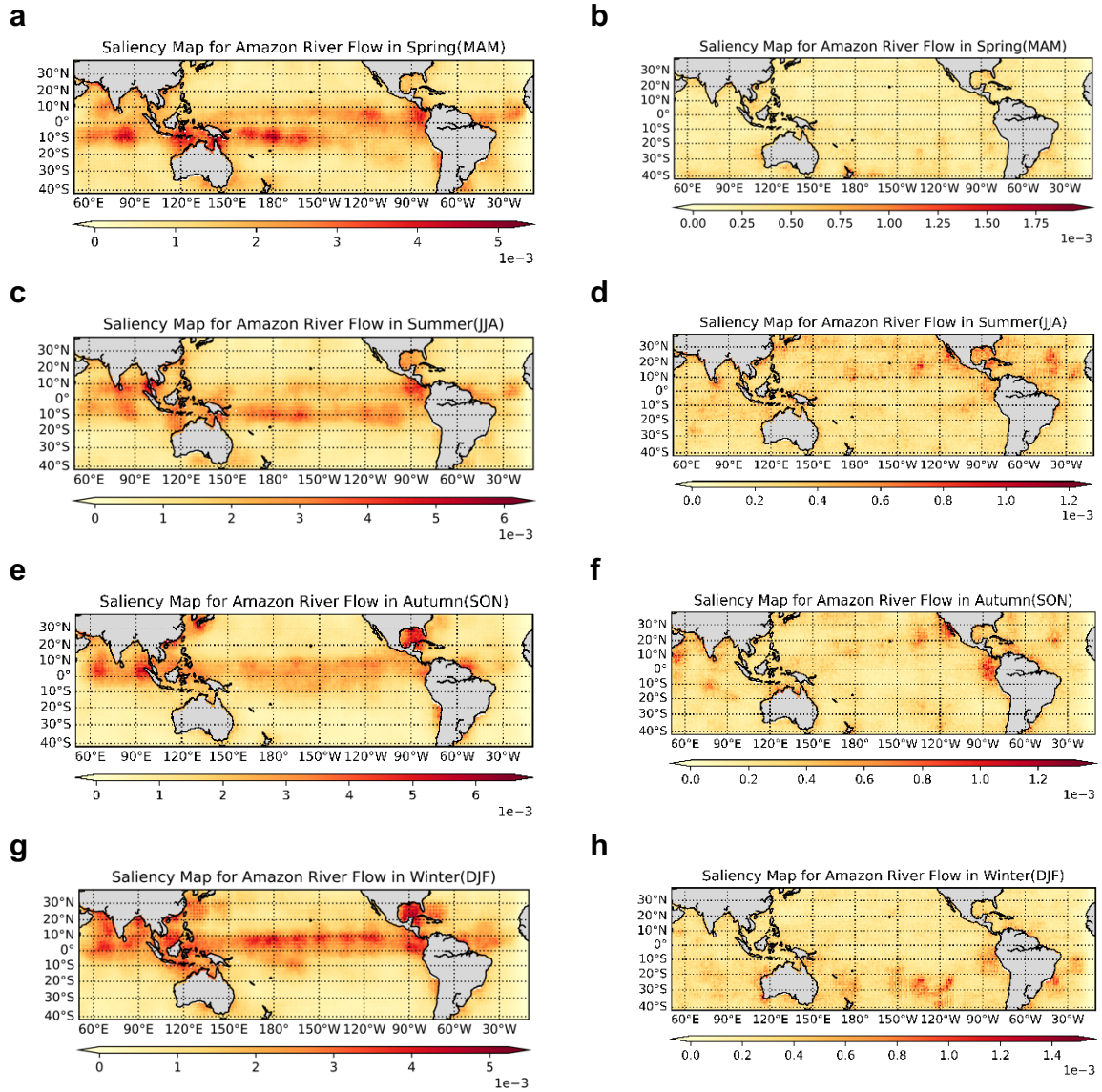


Figure S3. Seasonal cyclical saliency maps for predicting Amazon river flow using ESM (a,c,e,g) and reanalysis (b,d,f,h) SST. The seasonal cyclical saliency maps are calculated as the mean of saliency maps for different seasons (e.g., December, January and February for Spring; March, April and May for Summer, etc).

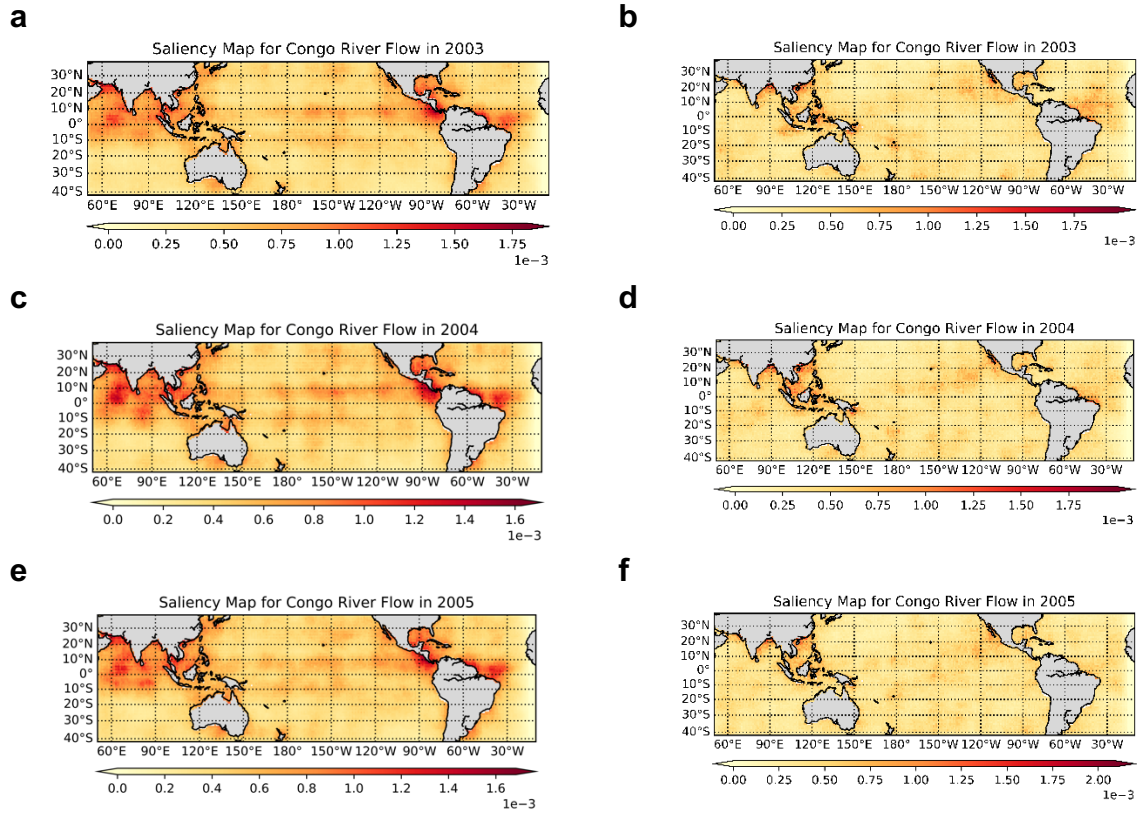


Figure S4. Yearly cyclical saliency maps for predicting Congo river flow using ESM (a,c,e) and reanalysis (b,d,f) SST. The yearly cyclical saliency maps are calculated as the mean of saliency maps of the 12 months in the corresponding year.

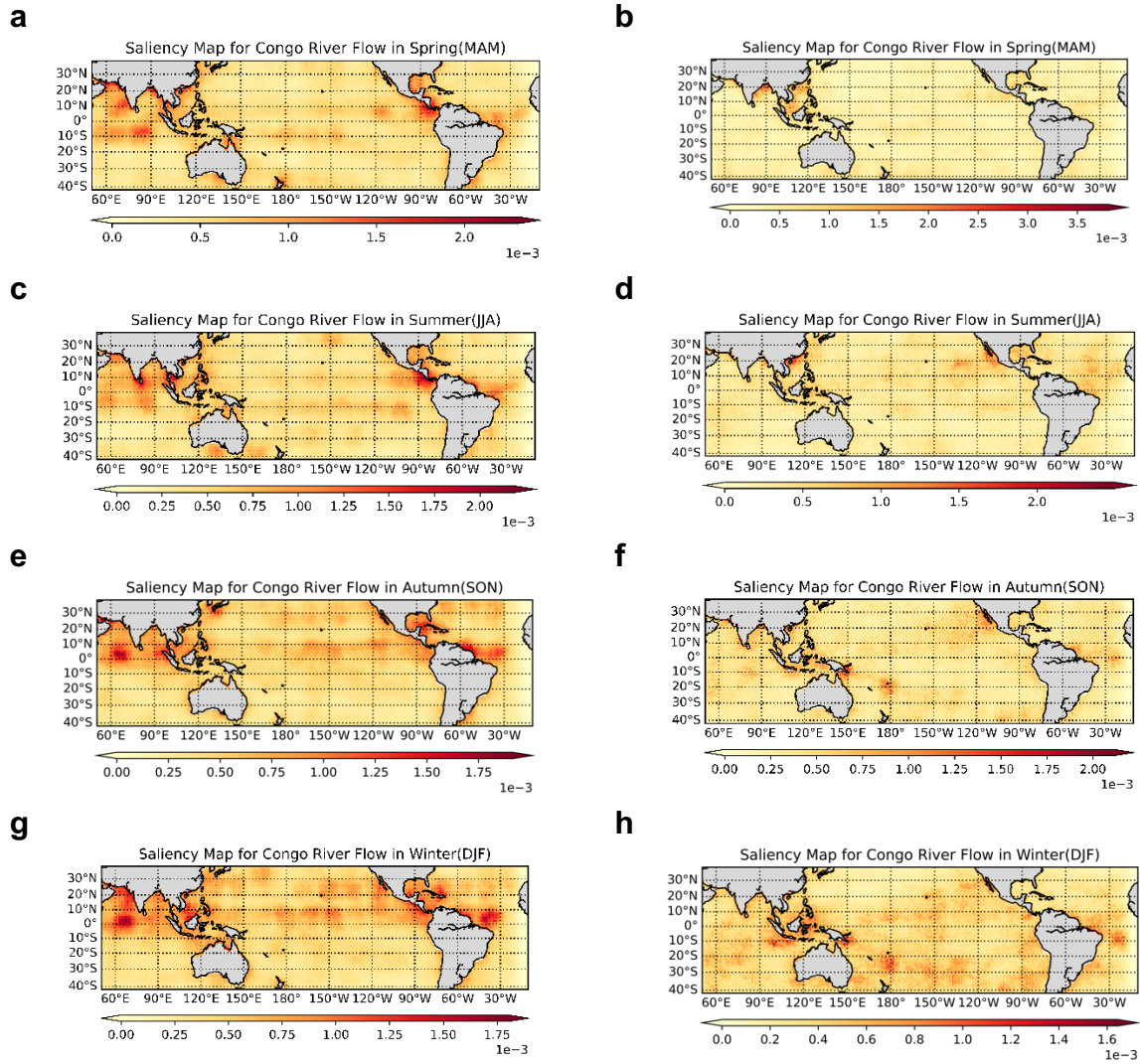


Figure S5. Seasonal cyclical saliency maps for predicting Congo river flow using ESM (a,c,e,g) and reanalysis (b,d,f,h) SST. The seasonal cyclical saliency maps are calculated as the mean of saliency maps for different seasons (e.g., December, January and February for Spring; March, April and May for Summer, etc.).

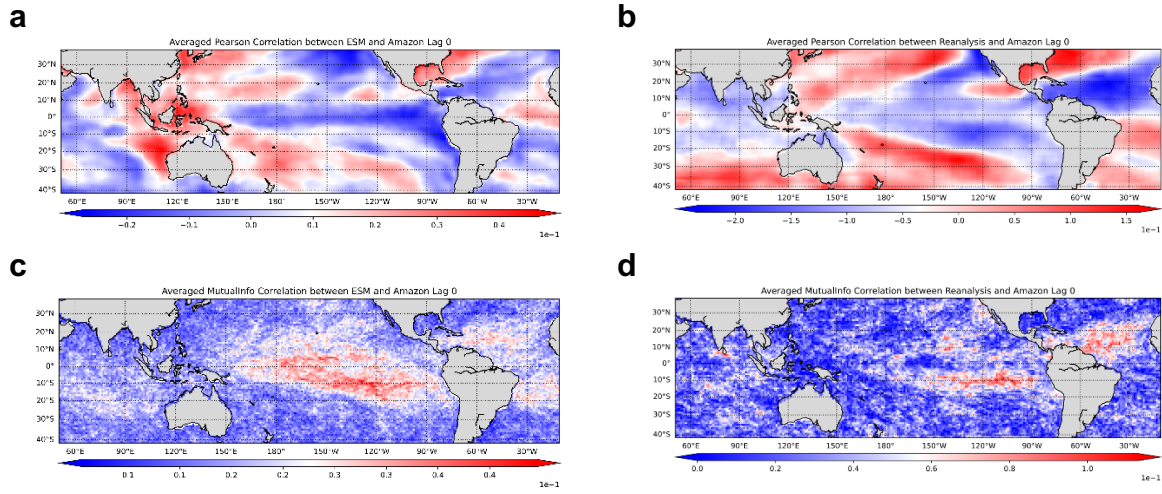


Figure S6. Correlation between Amazon river flow and ESM (a,c) and reanalysis SST (b,d). a,b, (linear) Pearson correlation. **c,d,** (nonlinear) Mutual information. The correlation is calculated between SST time series at each location with river flow time series. The time period is 672 months (from January 1950 to December 2005). We standardize the data for each natural month before calculating correlation.

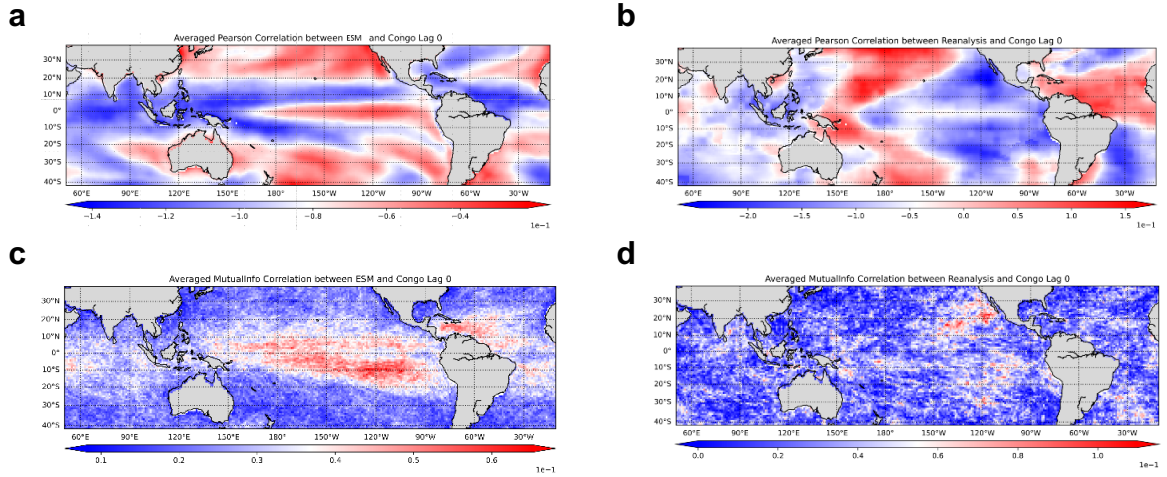


Figure S7. Correlation between Congo river flow and ESM (a,c) and reanalysis SST (b,d). a,b, (linear) Pearson correlation. c,d, (nonlinear) Mutual information. The correlation is calculated between SST time series at each location with river flow time series. The time period is 672 months (from January 1950 to December 2005). We standardize the data for each natural month before calculating correlation.

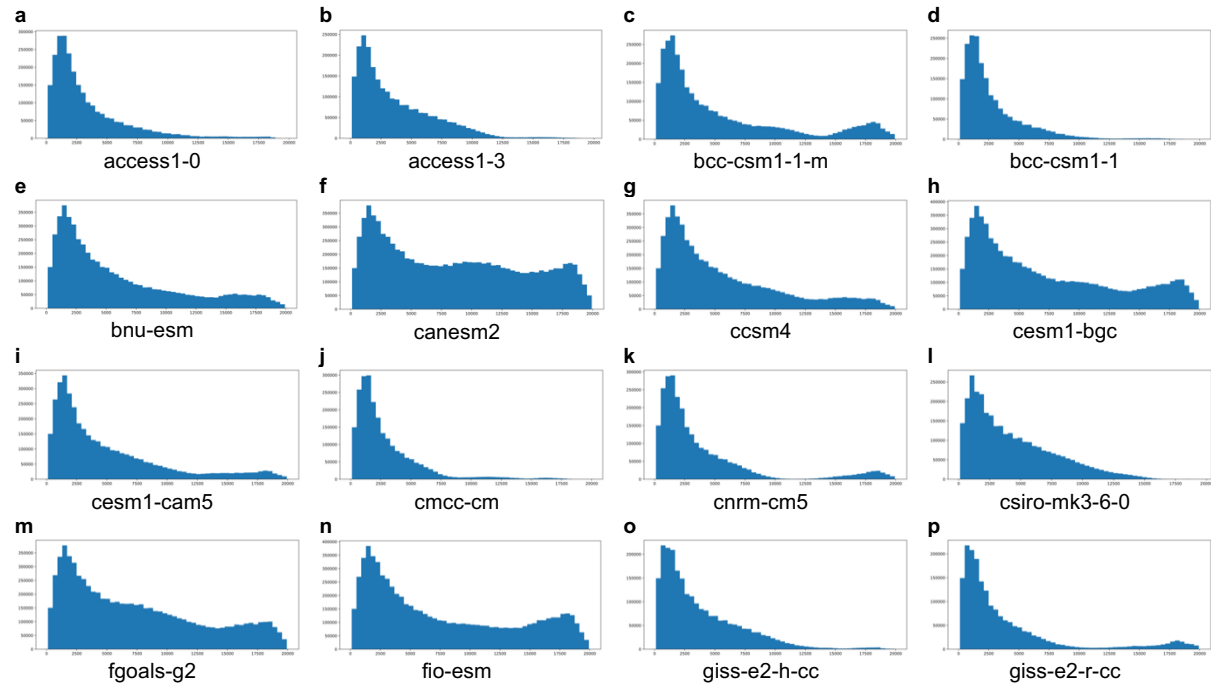


Figure S8. Histogram for distance with correlation above 0.5 for each ESM. We decide that there is a connection between two locations with some distance if the Pearson correlation between the SST time series at these locations is equal or larger than 0.5. The time period for SST is 672 month (from January 1950 to December 2005). We standardize the data for each natural months before calculating correlation. All locations lie in the area with latitude 9.5N to 9.5S and longitude 50.5E to 349.5E.

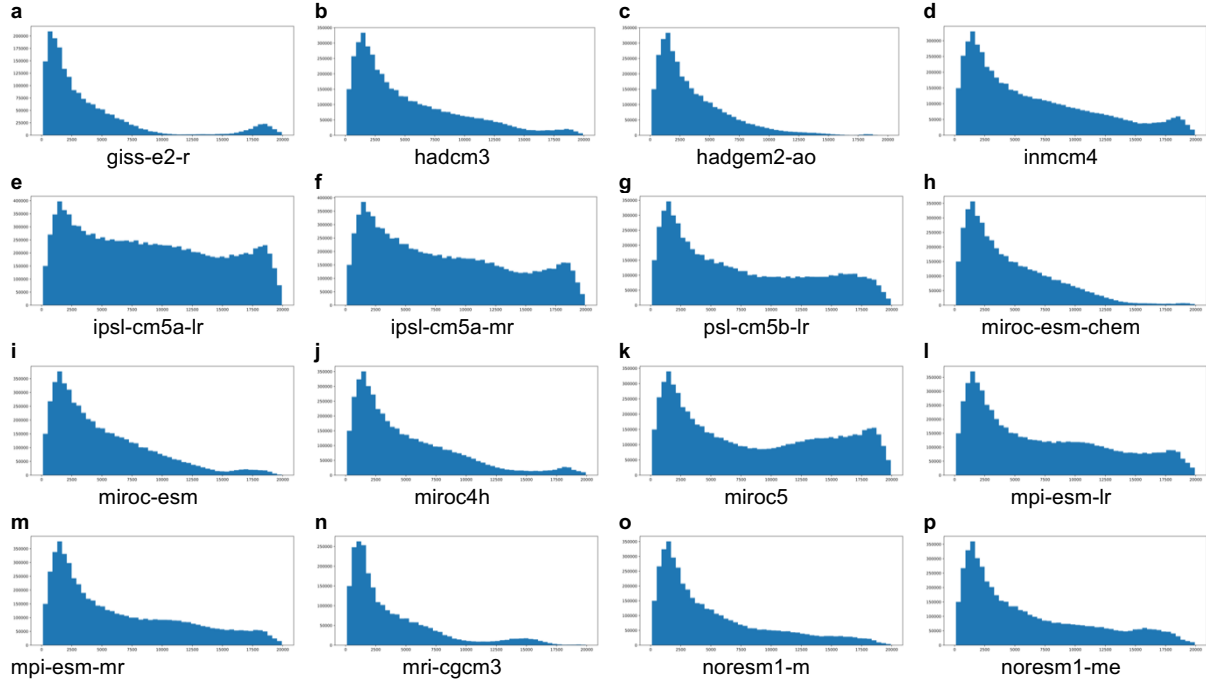


Figure S9. Histogram for distance with correlation above 0.5 for each ESM (continued). We decide that there is a connection between two locations with some distance if the Pearson correlation between the SST time series at these locations is equal or larger than 0.5. The time period for SST is 672 month (from January 1950 to December 2005). We standardize the data for each natural months before calculating correlation. All locations lie in the area with latitude 9.5N to 9.5S and longitude 50.5E to 349.5E.

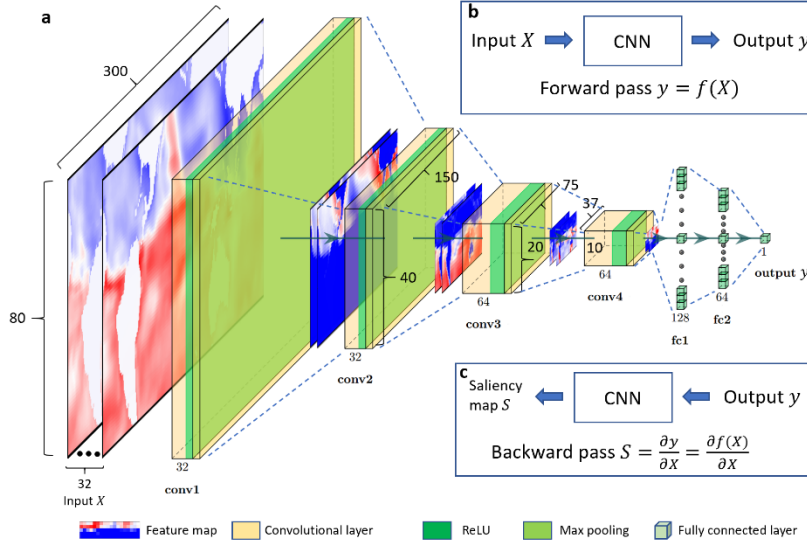


Figure S10. Architecture of CNN model used in this paper. **a**, network architecture. There are 4 convolutional layers (conv1 - conv4) and 3 fully connected layers (fc1,2 and output). Each convolutional layer is followed by a ReLU activation ($\text{ReLU}(x) = \max(0, x)$) and a max pooling layer. The image input size is $80 \times 300 \times C$ with $C = 1, 3$ or 32 depending on the datasets. For the convolutional layers, the filter sizes are all 3×3 with stride 1 and padding 1; and the number of filter channel is 32, 32, 64 and 64, respectively. The pooling layers are 2D max pooling layers with size 2×2 and will reduce the feature maps to half size. The outputs of the fully connected layers are 1D vectors with length 128, 64 and 1, respectively. **b**, forward pass to input climate variable SST as X and get prediction y . **c**, backward pass to calculate gradient of prediction y with respective to input X to get saliency maps.

Table S1. Earth system models used in the experiment.

Index	Name	Index	Name	Index	Name	Index	Name
0	access1-0	8	cesm1-cam5	16	giss-e2-r	24	miroc-esm
1	access1-3	9	cmcc-cm	17	hadcm3	25	miroc4h
2	bcc-csm1-1-m	10	cnrm-cm5	18	hadgem2-ao	26	miroc5
3	bcc-csm1-1	11	csiro-mk3-6-0	19	inmcm4	27	mpi-esm-lr
4	bnu-esm	12	fgoals-g2	20	ipsl-cm5a-lr	28	mpi-esm-mr
5	canesm2	13	fio-esm	21	ipsl-cm5a-mr	29	mri-cgcm3
6	ccsm4	14	giss-e2-h-cc	22	ipsl-cm5b-lr	30	noresm1-m
7	cesm1-bgc	15	giss-e2-r-cc	23	miroc-esm-chem	31	noresm1-me

Table S2. RMSE for predicting Amazon and Congo river flow using index and larger area SST.

Numbers with red bold and bold font indicate the best and second-best results; and numbers with * indicate best results when using indices as predictors.

Method		Linear, lasso, ridge, elastic net, random forest and DNN regression					Historical average		CNN	
Predictor type		Nino 3.4 index (C-dimensional time series, C=1, 3 or 32)					Climatological		SST (2-dimensional images)	
Predictor source		ESM mean	ESM	HadISST1	Reanalysis mean	Reanalysis	Historical mean	ESM	Reanalysis	
Amazon	Linear	1.051	0.508	0.925*	0.919*	0.925*	0.294	0.265	0.313	
	Ridge	1.047	0.499	0.925*	0.920	0.925*				
	Lasso	1.050	0.576	0.925*	0.919*	0.925*				
	Elastic net	1.028	0.469*	0.925*	0.922	0.925*				
	Random forest	1.216	0.518	0.958	1.002	0.943				
	DNN	1.002*	0.516	0.954	0.929	0.954				
	Ensemble	1.049	0.461	0.931	0.925	0.928				
Congo	Linear	1.012*	0.802	0.996*	0.976*	0.987	0.476	0.485	0.598	
	Ridge	1.012*	0.784	0.996*	0.977	0.985*				
	Lasso	1.022	0.848	0.996*	0.976*	1.000				
	Elastic net	1.022	0.799	0.996*	0.976*	0.993				
	Random forest	1.240	0.804	1.074	1.089	1.108				
	DNN	1.025	0.711*	1.000	0.980	0.980				
	Ensemble	1.043	0.750	1.005	0.992	0.999				

Table S3. Correlation between Nino indices and river flows.

Index		ESM mean	HadISST1	Reanalysis mean
Amazon	Pearson correlation	-0.0561	-0.191	-0.146
	Mutual information	0.049	0.077	0.077
Congo	Pearson correlation	-0.195	-0.024	-0.091
	Mutual information	0.058	0.008	0.097

Table S4. Different metrics for three prediction results for Amazon river. For Pearson, Spearman and Kendall's Tau correlation, the values in the parenthesis is the correlation and p-value, respectively. For the seasonal RMSE, the values in the parenthesis is RMSE for spring (DJF), summer (MAM), autumn (JJA) and winter (SON), respectively. For the yearly RMSE, the values in the parenthesis is RMSE for the year 2003, 2004 and 2005, respectively. For the extreme RMSE, the values in the parenthesis is RMSE for predictions whose absolusion values are within and outside 2 standard deviations, respectively. For above/below RMSE, the values in the parenthesis is RMSE for predictions whose values are above and below the mean (0), respectively. For ENSO RMSE, the values in the parenthesis is RMSE for warm, cool and neutral months, respectively.

Metric Method	Historical average	ESM+CNN	Reanalysis+CNN
Pearson correlation	(0.9637, 4.426e-21)	(0.967, 9.217e-22)	(0.9451, 4.397e-18)
Spearman correlation	(0.9504, 8.029e-19)	(0.9681, 5.171e-22)	(0.9284, 3.475e-16)
Kendall's tau correlation	(0.8402, 2.067e-12)	(0.8635, 1.265e-13)	(0.7778, 2.485e-11)
Mutual information	1.2425	1.2292	1.1371
Seasonal RMSE	(0.1695, 0.2220, 0.2407, 0.4576)	(0.2830, 0.2167, 0.1109, 0.3759)	(0.1941, 0.1722, 0.2789, 0.4956)
Yearly RMSE	(0.1728, 0.2338, 0.4177)	(0.2904, 0.2362, 0.2652)	(0.2382, 0.1717, 0.4548)
Extreme RMSE	(0.2622, 0.3145)	(0.2773, 0.2545)	(0.3339, 0.2998)
Above/below RMSE	(0.2815, 0.3057)	(0.2058, 0.3083)	(0.2961, 0.3281)
ENSO RMSE	(0.2040, 0.5991, 0.2868)	(0.2794, 0.2333, 0.2611)	(0.1820, 0.6420, 0.3136)
MAE	0.2215	0.2078	0.2382
Nash–Sutcliffe coefficient	0.9053	0.9231	0.893

Table S5. Different metrics for three prediction results for Congo river.

Metric Method	Historical average	ESM+CNN	Reanalysis+CNN
Pearson correlation	(0.909, 1.792e-14)	(0.8726, 4.051e-12)	(0.8994, 9.031e-14)
Spearman correlation	(0.8544, 3.397e-11)	(0.8682, 6.962e-12)	(0.86, 1.826e-11)
Kendall's tau correlation	(0.6866, 9.2312e-09)	(0.6921, 2.873e-09)	(0.673, 7.683e-09)
Mutual information	0.7301	0.5913	0.7445
Seasonal RMSE	(0.4908, 0.4468, 0.5885, 0.3440)	(0.9007, 0.4162, 0.3427, 0.5716)	(0.5257, 0.4639, 0.5788, 0.3400)
Yearly RMSE	(0.4866, 0.5178, 0.4171)	(0.8148, 0.4889, 0.4105)	(0.5434, 0.4873, 0.4172)
Extreme RMSE	(0.4122, 0.4874)	(0.4217, 0.6528)	(0.4417, 0.4971)
Above/below RMSE	(0.4612, 0.4858)	(0.8170, 0.4494)	(0.4985, 0.4758)
ENSO RMSE	(0.6421, 0.3819, 0.3943)	(0.7951, 0.5438, 0.4976)	(0.6423, 0.2926, 0.4176)
MAE	0.3879	0.4765	0.3895
Nash–Sutcliffe coefficient	0.7783	0.65	0.7691